Boosting hydrogen evolution via integrated construction and synergistic cooperation of confined graphene/CoSe$_2$ active interfaces and 3D graphene nanomesh arrays

Kai Chi [a,1], Zhu Wu [a,1], Xin Tian [a], Zhuoping Wang [a], Fei Xiao [a], Junwu Xiao [a], Shuai Wang [a,b,*]

[a] *Key Laboratory of Material Chemistry for Energy Conversion and Storage, Ministry of Education, Department of Chemistry and Chemical Engineering, Huazhong University of Science and Technology, Wuhan 430074, PR China*
[b] *State Key Laboratory of Digital Manufacturing Equipment and Technology, Flexible Electronics Research Center, Department of Mechanical Science and Engineering, Huazhong University of Science and Technology, Wuhan 430074, PR China*

ARTICLE INFO

ABSTRACT

Integrated fabrication and synergistic cooperation between active sites and carrier are expected to hunt non-precious electrocatalysts with high efficiency and durability for hydrogen evolution. Herein, the synthesis of N-doped graphene-confined hollow CoSe$_2$ nanoparticles (NG-HCS) anchored on N-doped vertically oriented graphene nanomesh arrays (NGM-As) on carbon cloth (CC/NG-HCS@NGM-As) is described. The graphene nanomesh arrays structure offers rich channels for fast ion/electron transportation and increases the contact area between electrolyte and electrodes. The unique graphene-confined structure not only protects the active sites against pulverization and wastage but also induces the charge transfer, penetration, and rearrangement processes to optimize the adsorption ability of hydrogen. These advantages enable the hybrid electrode to exhibit outstanding hydrogen evolution reaction performance, with a low overpotential of 133 mV at a current density of 10 mA cm^{-2} in alkaline media. This research opens a new avenue for the rational design of efficient electrocatalysts.

1. Introduction

As an important hydrogen production technology, the electrochemical hydrogen evolution reaction (HER) has attracted considerable attention because of its essential role in renewable and sustainable energy technology systems [1,2]. Platinum-based materials are currently recognized as the best electrocatalyst for HER, but their expensive price and scarcity make them difficult for large-scale commercial use [3]. Therefore, a considerable amount of alternative non-noble metal electrocatalysts are constantly emerging [4,5]. Among them, the representative transition metal selenides (TMSes) such as NiSe$_2$ [6], MoSe$_2$ [7–10], CoSe$_2$ [11–14], etc., have received extensive research as novel electroactive materials for HER due to their unique morphology, physical, and chemical properties. An electrocatalyst that can be used as a competitive candidate for massive-scale hydrogen production should have the following features, including high intrinsic activity, rapid

charge/mass transfer channel, accessible electroactive surface area, suitable surface wettability, and robust and stable structure [15,16]. While impressive progress has been made in improving individual features [17,18], few reports have focused on the synergistic enhancement of them. Therefore, it is urgent to develop a comprehensive, systematic, and multiscale control strategy for functionality integration towards efficient, stable, and affordable non-noble metals-based HER electroactive materials.

Fundamentally, the intrinsic activity of the catalyst determines the efficiency of hydrogen evolution. Therefore, the structural design of the catalytic site at the atomic scale and the adjustment of the local electronic structure are highly demanded for the effective decomposition of the water molecules during the catalytic process [19,20]. Till now, interfacial electronic modulation strategy is one of the possible solutions. Optimizing the interfacial electronic coupling structure, such as metal-support interactions adjusting [21], heterojunction interface

construction [22], interfacial covalent bonds regulating [23] etc., can finely tune their electronic states and active sites, thereby, improving the catalytic activity. Impressively, researchers coupled electroactive materials with carbon-based conductive materials e.g., carbon nanotube, graphene, and porous carbon to construct a confined carbon/-electroactive material active interface [24,25]. This hybrid interface yields profound enhancement effects on its electrocatalytic activity, conductivity and stability improvement. For instance, Bao et al. proposed a combination of the active species and the conductive matrix as a core-shell spatially confined structure, which subsequently has been widely used in various materials [26,27]. This structure induces the recurrence of charge distribution at the coupling interface. Such charge recurrence leads to a synergistic effect to improve the conductivity and adsorption ability for the reactants, enhancing the electrocatalytic activity. Furthermore, the sturdy shell structure has outstanding protection and cushioning effect and subsequently improves the chemical and structure stability during the HER process.

Moreover, the rapid catalysis process results in the swift consumption of electrolytes and the rapid production of bubbles. Thus, the rapid mass transfer rate is particularly important, where the electrolyte needs to be replenished immediately and the bubbles are quickly effluxed [28, 29]. However, the traditional solid catalyst has a large particle size and inherently lacks a reasonable hierarchical pore distribution. As such, catalysts are accumulated and covered by each other when constructing the catalyst coating. Such an accumulation not only seriously hinders the mass transfer process but also significantly reduces the utilization of active sites [30,31]. To solve these problems, researchers have developed multiple feasible routes to fabricate self-supporting electrodes by shaping active materials into various well-aligned 3D nanoarray morphologies (i.e., nanosheets [32], nanowires [33], and nanotubes[34]) on the current collector, or embedding/loading active materials on a carrier with specific nanoarray architectures [35–37]. 3D nanoarrays architecture possesses relatively ordered, continuous, and fully exposed active surfaces, maximizing active site exposure, creating more active reaction sites and increasing the electrode-electrolyte contact area, expecting to further improve their electrochemical activity. Meanwhile, some literatures indicate that the surface of the array structure has superaerophobic and superhydrophilic properties, which can speed up electrolyte replenishment and bubble overflow [38,39]. As a member of the array carrier family, vertically aligned graphene nanosheet arrays (VAGNAs) possess favorable electrical conductivity, large surface area, and unique 3D interconnected structures. These features make VAGNAs as an appropriate support for active materials loading to construct self-supporting electrodes [40,41]. In particular, the vertically aligned N-doped graphene nanomesh array (VNGNMA) reported earlier by our research group not only inherits the excellent characteristics of VAGNAs, but also has abundant in-plane pores that can facilitate electron/ion accessibility to active sites [42].

Inspired by the aforementioned considerations, combination of electronic modulation and nanostructural design to form a self-supporting integrated electrode is a powerful method for improving electrochemical performance and stability. Herein, an easy and stepwise strategy, with a template-assisted process followed by conventional selenization treatment, is developed to synthesize N-doped graphene-confined hollow $CoSe_2$ nanoparticles anchored on N-doped vertically oriented graphene nanomesh arrays grown on carbon cloth (CC/NG-HCS@NGM-As). The obtained CC/NG-HCS@NGM-As exhibits optimal HER catalytic performance in alkaline media. Advanced characterizations and calculations reveal the superiority of synergistic cooperation. On the one hand, the ultrathin N-graphene shells strongly promote electron penetration from the $CoSe_2$ nanoparticles to the N-graphene surface, the interfacial charge modulation could intrinsically optimize the adsorption of H* , accelerating the reaction kinetics. On the other hand, 3D graphene nanomesh arrays expedites mass transport and bubble slippage. This work provides a valuable insight toward advanced non-noble metal-based electrocatalysts for efficient alkaline HER.

2. Experimental section

2.1. Preparation of CC/NG-HCS@NGM-As

First, a three-electrode electrochemical device was used to deposit $Co(OH)_2$ nanosheet array on CC in which the following were used: platinum foil as the counter electrode, Ag/AgCl as the reference electrode, a piece of carbon cloth (1 cm × 2 cm) as the working electrode, and 0.05 M $Co(NO_3)_2$ solution as the electrolyte. The deposition occurred at a constant potential of − 1.0 V vs. Ag/AgCl for 10 min to obtain CC/CH-As. Second, CC/CH-As was dipped into an aqueous Tris (hydroxymethyl) aminomethane (Tris) solution containing dopamine (2 mg of dopamine per mL of 10 mM Tris, pH ∼ 8.5). After 24 h, the product (CC/CH@PDA-As) was removed from the solution and washed with deionized (DI) water. Third, a piece of CC/CH@PDA-As was directly annealed at 600 °C for 1 h under an argon atmosphere to obtain CC/Co@NGM-As. Finally, a piece of CC/Co@NGM-As was annealed at 400 °C for 3 h in Se vapor under an argon atmosphere, with 1 g of Se powder at the upstream side of a tube furnace.

2.2. Preparation of comparative samples

The preparation process of the comparative samples is shown in Fig. S1. Typically, a piece of CC/Co@NGM-As was immersed into a 3 M HCl solution for 24 h then washed with DI water and dried at 60 °C overnight, finally fabricating the CC/NGM-As. A piece of CC/CH-As was directly annealed at 400 °C for 3 h in Se vapor under an argon atmosphere to obtain CC/CS-As.

3. Results and discussion

3.1. Preparation and characterization

As illustrated in Fig. 1, the synthetic procedure for the self-supporting and flexible CC/NG-HCS@NGM-As electrode encompasses four major steps. First, the $Co(OH)_2$ nanosheet arrays with smooth surfaces were directly deposited onto carbon cloth by a cathodic deposition method, denoted as CC/CH-As. Second, the polydopamine (PDA) layer was deposited onto the CH-As via a typical self-polymerization process, which conserves the morphology and crystal phase of the $Co(OH)_2$ nanosheet arrays, as determined by scanning electron microscopy (SEM) and X-ray diffraction (XRD) characterization (Figs. S2 and S3). Third, the CC/CH@PDA-As was annealed under an argon atmosphere to form metallic cobalt@nitrogen-doped graphene nanomesh nanoarrays (CC/Co@NGM-As) via our previously reported diffusing–disembedding–graphitizing mechanism [42], also proved by transmission electron microscopy (TEM) images (Fig. S4). Finally, the CC/Co@NGM-As was selenized by the fumigation method in the presence of selenium sources, generating nitrogen-doped graphene-confined hollow $CoSe_2$ nanoparticles (NG-HCS) anchored on nitrogen-doped vertically oriented graphene nanomesh arrays (CC/NG-HCS@NGM-As). For comparison, CC supported $CoSe_2$ nanosheet arrays (CC/CS-As) sample was also fabricated by a similar selenizion method using CC/CH-As as the precursor (Figs. S5 and S6).

The morphological and microstructural details of CC/NG-HCS@NGM-As were probed using SEM and TEM. As shown in Fig. 2a, the NG-HCS@NGM-As composite is uniformly grown over the entire surface of the carbon cloth. It possesses a vertically erect and robust nanosheet structure (with a thickness of ∼100 nm, Fig. 2b and c), which favors speedy ion/electron transmission and enlarges the contact area between electrolyte and electrodes. The TEM images in Fig. 2d reveal that $CoSe_2$ nanoparticles are embedded in the NGM nanosheet, consistent with the SEM results. Fig. 2e demonstrates $CoSe_2$ nanoparticles with a hollow structure, with diameters of ∼500 nm and wall thicknesses of ∼100 nm. The formation of hollow $CoSe_2$ nanoparticles can be explained by the nanoscale Kirkendall effect [43]. Furthermore, in-plane
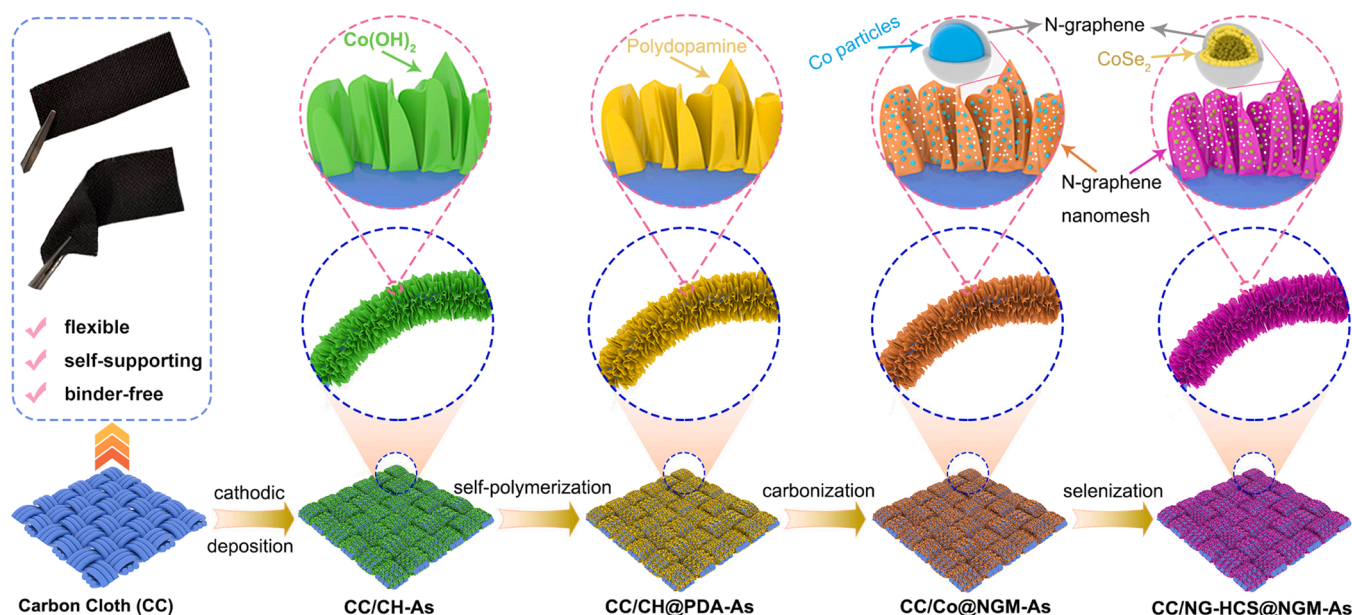
Fig. 1. Schematic illustration of the synthetic route of the CC/NG-HCS@NGM-As.

holes with diameters of ~10–20 nm are clearly observed in the NGM (Fig. 2f). It is noteworthy that the NGM nanosheets not only ensure efficient electron transfer but also provide a wealth of fast channels for mass transfer along the Z-axis of the two-dimensional nanosheet plane. As can be observed from the magnified view image (Fig. 2g), hollow CoSe₂ nanoparticles are tightly encapsulated within ultrathin nitrogen-doped graphene shells with high crystallinity. With the graphene as a bond or link, the unique graphene-confined structure of NG-HCS nanohybrids is integrated with the two-dimensional sheet-like GNM structure. The high-resolution TEM image (Fig. 2h) reveals interplanar spacing of 0.262 nm and 0.186 nm, which are assigned to the orthorhombic CoSe₂ crystal planes of (111) and (220), respectively, as also confirmed by the line scan of the TEM image (Fig. 2i and j). Elemental mapping images in Fig. 2k further verify the homogeneous distribution of C and N signals over the NG-HCS@NGM composite, as well as the Co and Se signals of the hollow CoSe₂ particles.

The composition and chemical state of CC/NG-HCS@NGM-As was characterized by various techniques, as shown in Fig. 3. XRD pattern indicates that the as-synthesized CC/NG-HCS@NGM-As are composed of mixed orthorhombic (JCPDS card no. 53–0449) and cubic (JCPDS card no. 65–3327) CoSe₂ phases (Fig. 3a) [44]. Moreover, the broad peak at around 26° is related to the (002) plane of graphene [44]. Fig. 3b displays the Raman spectra of CC/NG-HCS@NGM-As. The peaks at 188.0 and 663.5 cm⁻¹ are attributed to the A_g and $A_{1 g}$ modes of CoSe₂, respectively, and the weak peaks at 462.7, 505.5, and 601.3 cm⁻¹ are assigned to the E_g, $F_{2 g}^1$, and $F_{2 g}^2$ modes of Co₃O₄, respectively, caused by surface oxidation [45]. The peaks located at 1341.0 and 1576.9 cm⁻¹ are attributed to the D band (sp^3 carbon) and G band (sp^2 carbon), respectively [45]. The I_D/I_G ratio is 0.99, indicating that the N-doped graphene shells have a high degree of graphitization, which is conducive to improving the electrical conductivity. The mass loading of CoSe₂ in CC/NG-HCS@NGM-As was evaluated using thermal gravimetric analysis (TGA). From the TGA curve (Fig. 3c), the weight loss starting at 315 °C results from the conversion of CoSe₂ into CoSeO₄ and SeO₂. The mass loss after 600 °C is a result of the transformation from CoSe₂ and CoSeO₄ to Co₃O₄, the sublimation of SeO₂, as well as the subsequent combustion of carbonaceous materials such as NG and CC [45,46]. Therefore, based on the final Co₃O₄ product, the amount of CoSe₂ in CC/NG-HCS@NGM-As is calculated to be 47.4 wt%.

The chemical states of CC/NG-HCS@NGM-As were examined using X-ray photoelectron spectroscopy (XPS). The total spectrogram (Fig. S7)

confirms the coexistence of C, N, Co, Se, and O elements in CC/NG-HCS@NGM-As, with atomic percentages of 68.9%, 7.2%, 5.4%, 12.1%, and 6.4%, respectively. For the C 1 s spectrum in Fig. 3d, three peaks located at 284.8, 286.2, and 288.1 eV can be attributed to sp^2 C, C–N/C═N, and C═O groups, respectively [47]. The N 1 s spectrum can be well fitted into three peaks at 398.7, 400.3, and 401.5 eV, corresponding to pyridinic N, pyrrolic N, and graphitic N, respectively (Fig. 3e) [47,48]. These evidences strongly confirm the doping of N atoms into the graphene matrix. The Co 2p spectrum (Fig. 3f) shows two broad peaks at 780.8 and 797.5 eV corresponding to Co^{2+} $2p_{3/2}$ and Co^{2+} $2p_{1/2}$, respectively [49]. The peaks at 778.7 and 793.6 eV correspond to Co^{3+} $2p_{3/2}$ and Co^{3+} $2p_{1/2}$, respectively, and are due to the partial surface oxidization of CoSe₂ in air, which corresponds with the results of previous studies on CoSe₂ [49,50]. The Se 3d spectra (Fig. 3g) can be deconvoluted into two main peaks at 54.9 and 55.7 eV, corresponding to Se $3d_{5/2}$ and $3d_{3/2}$ of Se^{2-}, respectively, which reveals the existence of CoSe₂ in CC/NG-HCS@NGM-As [50,51]. The additional peaks at 56.6, 58.8, 59.9, and 61.1 eV correspond to Se–Se bonds (due to residual trace metalloid Se), Co $3p_{3/2}$, Co $3p_{1/2}$, and Se–O bonds (due to partial oxidation at the composite surfaces), respectively [51].

The electrical conductivity (Fig. 3h) measured by four-point probe technology shows that the CC/NG-HCS@NGM-As electrode possesses a conductivity of ~44.0 S cm⁻¹, which is significantly higher than that of the corresponding CC/CS-As electrode (~36.7 S cm⁻¹). This result demonstrates that the introduction of nitrogen-doped graphene significantly improves the conductivity of the CC/NG-HCS@NGM-As composite electrode. In addition, the porosity properties of CC/NG-HCS@NGM-As were determined by N₂ adsorption/desorption method. The CC/NGM-As sample obtained by removing the Co nanoparticle templates was also measured as control. As shown in Fig. 3i, the pore size distribution of two samples exhibit broad pore size distribution of 2–200 nm and mainly centered at ~20 or ~100 nm, suggesting the existence of mesopores and macropores. Compared with CC/NGM-As, CC/NG-HCS@NGM-As sample shows a great decrease in pore volume. The reduced porosity can be attributed to the inner space once occupied by Co nanoparticles, which can be exposed by acid treatment in CC/NGM-As, while in CC/NG-HCS@NGM-As, the Co particles have been converted to CoSe₂ particles and still remain in their original position. Nevertheless, after excluding this part of the pores, CC/NG-HCS@NGM-As still has a high pore volume, which is mainly formed by the cobalt particles via diffusing–disembedding–graphitizing mechanism, and is
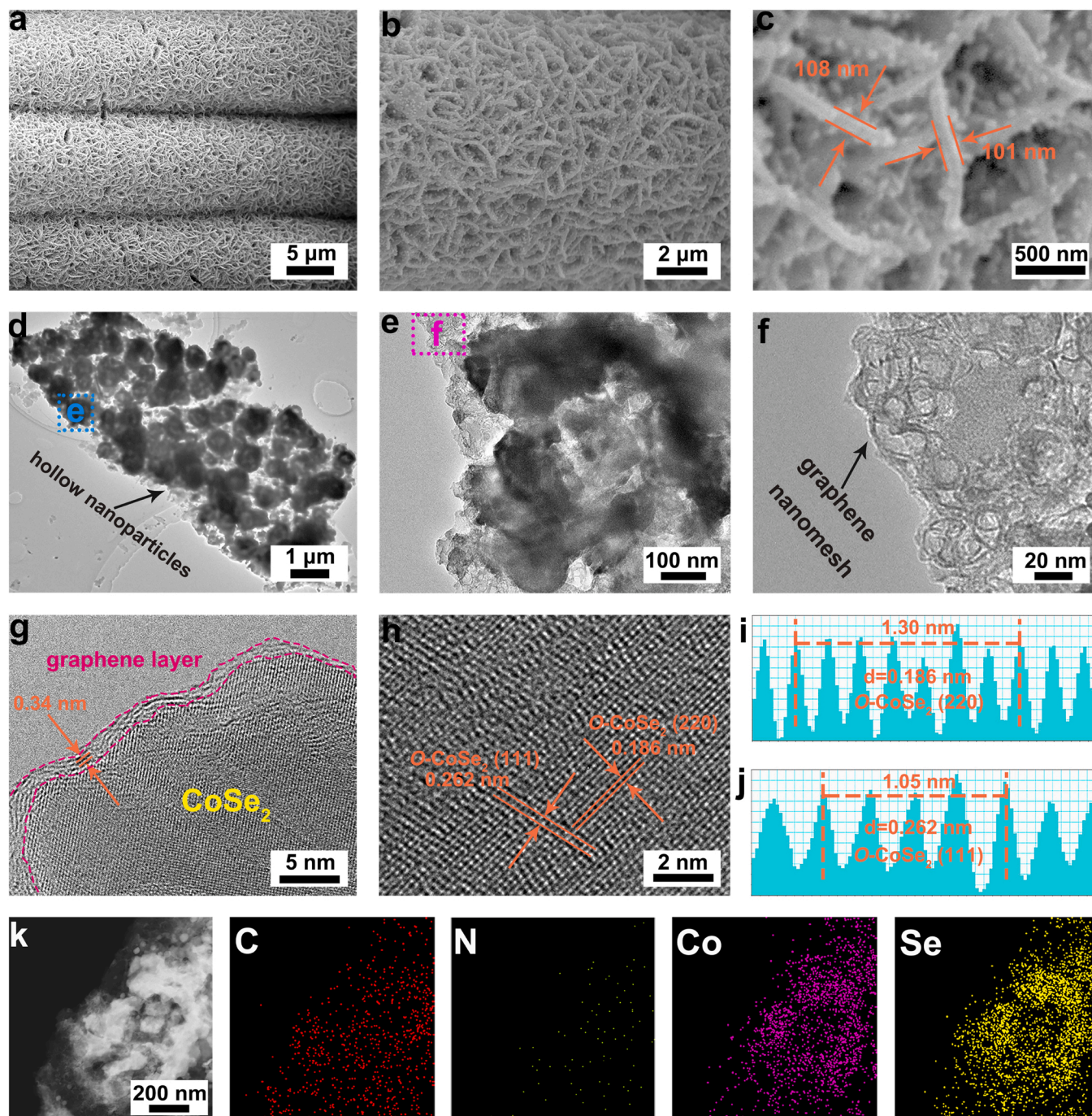
Fig. 2. (a-c) SEM images of CC/NG-HCS@NGM-As. (d-h) TEM and HRTEM image of NG-HCS@NGM. (i, j) Line scan of the HRTEM image. (k) Elemental mapping images of NG-HCS@NGM.

also the main source of pores in graphene nanomeshes. According to the above structural characterization, the proposed "integrated construction" concept was successfully realized, and the designed hybrid electrode was synthesized in the form of N-doped graphene-confined hollow CoSe$_2$ nanoparticles anchored into 3D vertically oriented graphene nanomesh arrays.

3.2. Electrochemical HER catalytic performances

To implement our proof-of-concept, the HER activity of CC/NG-HCS@NGM-As was evaluated using a three-electrode system in 1.0 M KOH. Bare CC, CC/NGM-As, CC/CS-As, and CC/Pt-C electrodes were examined for comparison. Fig. 4a presents the linear sweep voltammetry

(LSV) curves of these samples. Bare CC and CC/NGM-As electrodes displayed very poor HER performances. Except for CC/Pt-C electrode, CC/NG-HCS@NGM-As shows the lowest onset potential and fastly increasing HER polarization current response with the increasing of applied potentials. In contrast, at a current density of 10 mA cm^{-2}, CC/NG-HCS@NGM-As exhibited a substantial enhancement in hydrogen evolution activity with an overpotential of 133 mV, which is lower than that of CC/CS-As (194 mV) and CC/NGM-As (395 mV). The intuitive contrast of E$_{10}$ and E$_{100}$ is illustrated in Fig. 4b, highlighting the best HER activity of CC/NG-HCS@NGM-As among these counterparts. This significant improvement might originate from the effectual cooperative effect of two parts, one is the confined graphene/CoSe$_2$ active interfaces provided rich active sites, and the other is that 3D graphene nanomesh
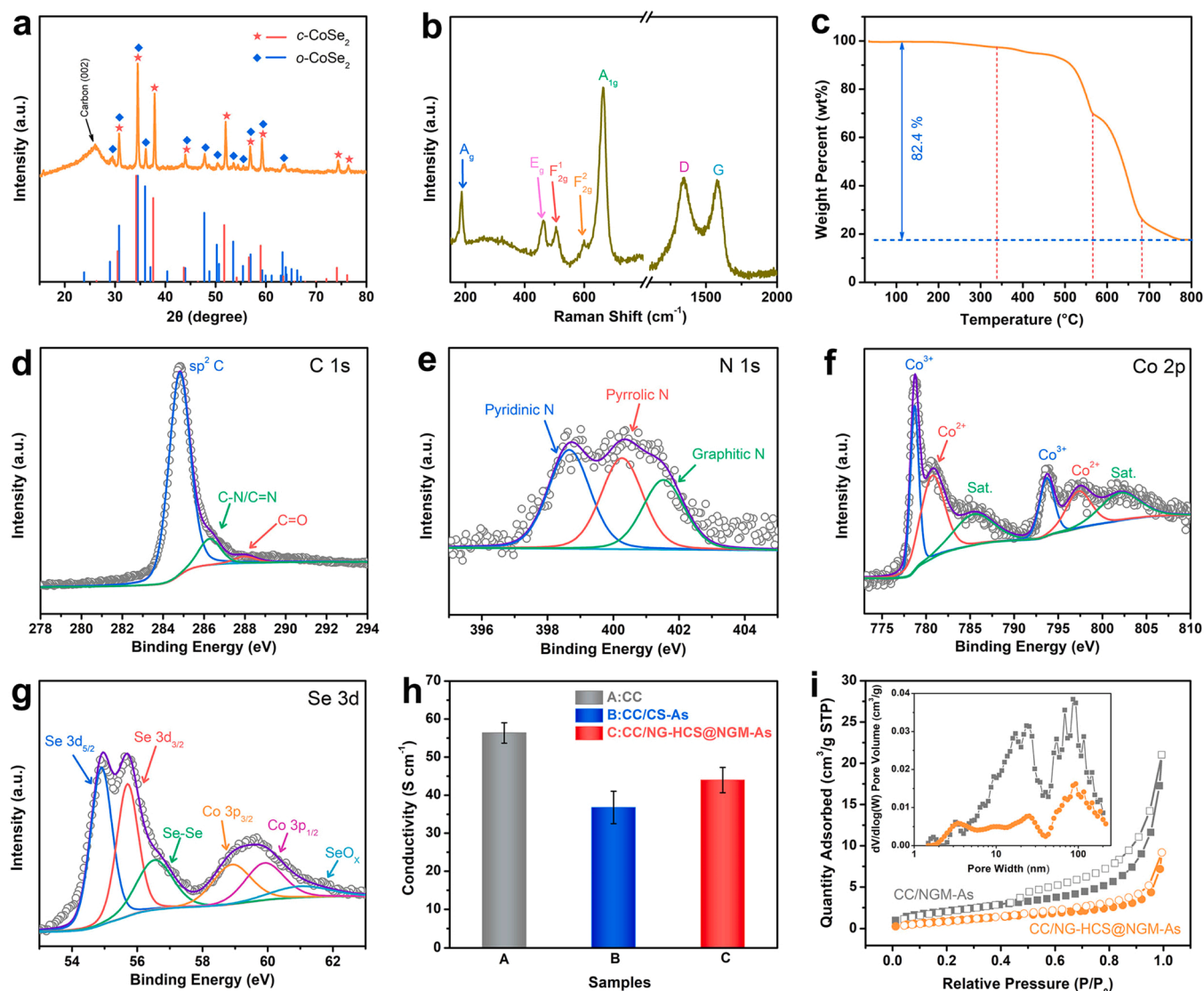
Fig. 3. (a) XRD patterns, (b) Raman spectrum, and (c) TGA curve of CC/NG-HCS@NGM-As. XPS spectra of CC/NG-HCS@NGM-As composite: (d) C 1 s, (e) N 1 s, (f) Co 2p, and (g) Se 3d. (h) The electronic conductivity of the CC/NG-HCS@NGM-As, CC/CS-As and bare CC samples. (i) N_2 adsorption-desorption isotherms and pore size distributions of CC/NGM-As and CC/NG-HCS@NGM-As samples.

arrays ensures efficient mass/electron transport. Tafel slopes derived from LSV curves were applied to assess the catalytic kinetics. As shown in Fig. 4c, the CC/NG-HCS@NGM-As electrode exhibited Tafel slopes of 80.5 mV dec^{-1}, which is slightly higher than Pt/C (42.5 mV dec^{-1}) but smaller than those of CC/CS-As (164.7 mV dec^{-1}) and CC/NGM-As (359.4 mV dec^{-1}). The value of CC/NG-HCS@NGM-As located between 40 and 120 mV dec^{-1}, not only indicates the fast electron transfer but also reveals Volmer-Heyrovsky HER mechanism in alkaline media. Based on the above analysis, the as-synthesized CC/NG-HCS@NGM-As exhibits the topmost HER activity, outperforming most $CoSe_2$ and Co metal-based electrocatalysts reported to date (Fig. 4d and Table S2). The Faradaic efficiency of the CC/NG-HCS@NGM-As is as high as 95% for HER (Fig. S9). Additionally, the turnover frequency (TOF) for these catalysts was calculated to describe the intrinsic activity. According to the estimated number of active sites (Fig. S10), the calculated TOF plots of these catalysts was shown in Fig. 4e. At the overpotential of 150 mV, CC/NG-HCS@NGM-As exhibits a TOF value of 0.15 s^{-1}, larger than that of CC/CS-As (0.06 s^{-1}), confirming the advance by the constructing confined graphene/$CoSe_2$ active interfaces and 3D graphene nanomesh arrays in hybrid system. The faster HER kinetics of the CC/NG-HCS@NGM-As electrode was further demonstrated by electrochemical

impedance spectroscopy (EIS) curves (Fig. 4f). Based on the equivalent circuit and corresponding fitting results (Table S3), the R_{ct} value of CC/NG-HCS@NGM-As is identified to be 18.8 Ω, which is much lower than that of CC/CS-As (60.0 Ω), demonstrating the much faster interfacial electron transfer kinetics of CC/NG-HCS@NGM-As during the HER process. The dramatic enhancement can be ascribed to the electron transfer from NG to $CoSe_2$ through interfacial contact. Moreover, The electrode's electrochemically active surface area (ECSA) was evaluated by electrochemical double-layer capacitance (C_{dl}), which is calculated based on the linear slope of the ΔJ/2 (from the cyclic voltammetry curves in Fig. S11) versus scan rate. As depicted in Fig. 4g, the C_{dl} value of CC/NG-HCS@NGM-As is 137.7 mF cm^{-2}, remarkably larger than that of CC/CS-As (60.2 mF cm^{-2}), which corroborates the significant increase of the reaction active sites for CC/NG-HCS@NGM-As.

Long-term stability is a crucial parameter for practical electrocatalysts. The LSV curve (Fig. 4h) obtained after 2000 CV cycles overlaps well with the initial curve, indicating the excellent stability of CC/NG-HCS@NGM-As electrode. Moreover, The exceptionally catalytic robustness was confirmed by maintaining a constant current density of 10 mA cm^{-2} over a 35 h period, during which CC/NG-HCS@NGM-As shows almost no voltage fading relative to the CC/CS-As catalyst
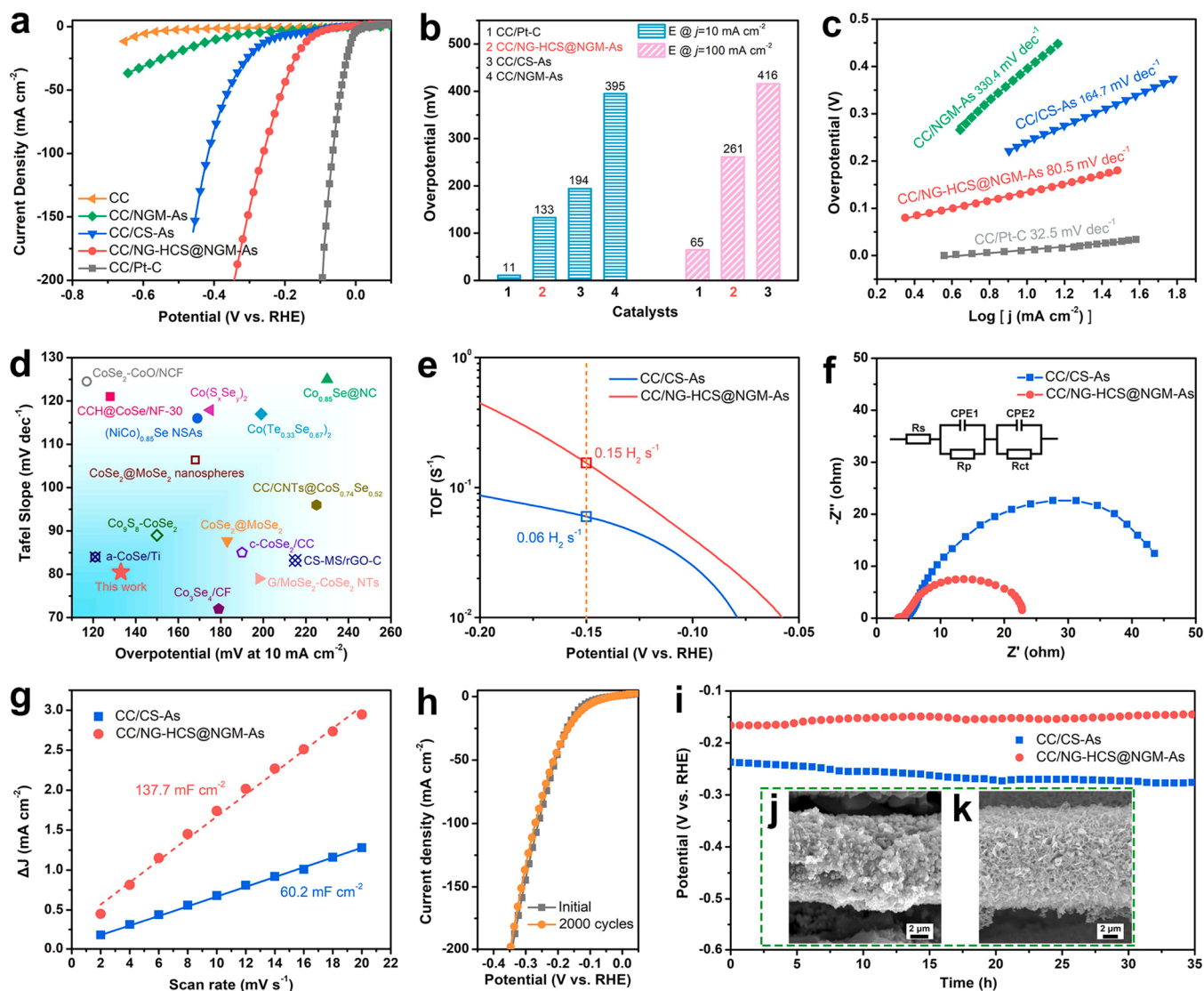
Fig. 4. (a) HER polarization curves of CC, CC/NGM-As, CC/CS-As, CC/NG-HCS@NGM-As, and CC/Pt-C. (b) The comparison of overpotentials required to achieve 10 and 100 mA cm^{-2} for various catalysts. (c) Corresponding Tafel slope originated from LSV curves. (d) Comparison of overpotentials at 10 mA cm^{-2} and Tafel slopes for CC/NG-HCS@NGM-As and recently reported advanced HER electrocatalysts. (e) TOFs plots and (f) Nyquist plots of CC/CS-As and CC/NG-HCS@NGM-As. (g) Plots of the current density versus the scan rate for CC/CS-As and CC/NG-HCS@NGM-As. (h) LSV curves of CC/NG-HCS@NGM-As before and after 2000 CV cycles. (i) Time dependence of potential curve of CC/CS-As and CC/NG-HCS@NGM-As recorded at a current density of − 10 mA cm^{-2}. SEM images of the (j) CC/CS-As and (k) the CC/NG-HCS@NGM-As electrodes after HER measurements.

(Fig. 4i). Subsequently, the morphological changes of the electrodes after the long-term HER test were examined using SEM. As shown in Fig. 4j and k, the nano-arrays morphology in the CC/NG-HCS@NGM-As electrode is well maintained, but the nanosheet arrays in CC/CS-As electrode have collapsed and peeled from the CC substrate, further revealing the excellent structural stability of CC/NG-HCS@NGM-As. According to the TEM results (Fig. S12), the main reason for such a phenomenon is that, the outer NG coating layer ensures the composite has a stable structure, which could effectively alleviate the volume changes and structural variation, thus hindering the pulverization of CoSe$_2$. Consistently, the phase structure and surface elemental composition of CC/NG-HCS@NGM-As were well maintained after continuous cathodic reaction, which were characterized by XRD and XPS (Figs. S13 and S14). The remarkable stability of CC/NG-HCS@NGM-As also demonstrates the effectiveness of structural design and the advantages of integrated fabrication.

3.3. DFT calculation and theoretical investigations

To understand the enhancement mechanism of HER performance in depth, we conducted the density function theory (DFT) calculations to determine the underlying synergistic effect between N-doped graphene shells and CoSe$_2$ cores. Three theoretical models were designed to simulate the CoSe$_2$ cluster encapsulated by one, two, or three NG layers. To investigate the charge distribution on this confined structure, Fig. 5a shows the charge density differences in side view. Obviously, the electrons are redistributed and penetrate the graphene layers after assembling the NG and CoSe$_2$ to confined structure. Taking the CoSe$_2$ couple with one N-doped graphene layer model as an example, changes in the density of states (DOSs) before and after NG coupling were compared. In Fig. 5b, for CoSe$_2$ @NG model, the coated NG is a conductor and contributes impurity energy levels to the band gap in which electrons can easily transfer along the NG [52]. Therefore, the CoSe$_2$ @NG has a faster electron transport rate and higher electrical conductivity than that of pure CoSe$_2$. The above results prove that the coupling of NG can provide
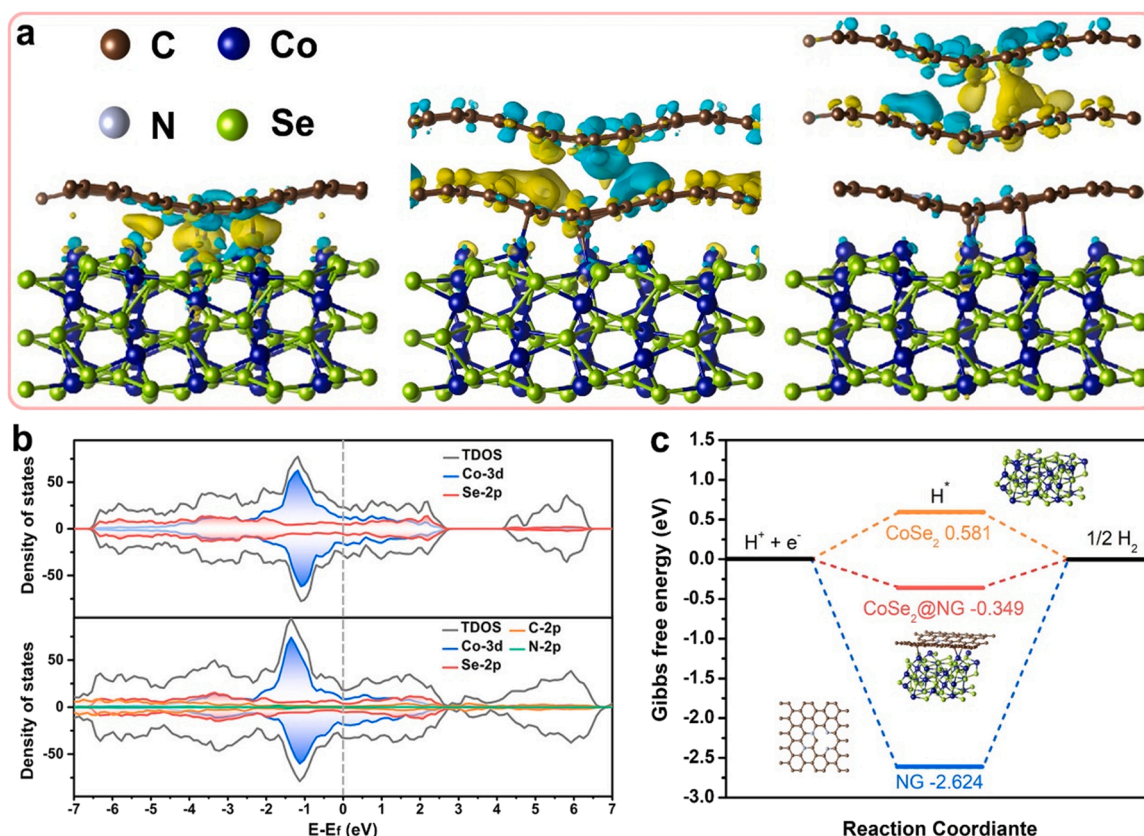
Fig. 5. (a) Redistribution of the electron densities after the CoSe$_2$ have covered by one to three layers of graphene. The yellow and blue regions are regions of increased and decreased electron density, respectively. (b) Calculated density of states (DOS) of CoSe$_2$ and CoSe$_2$ @NG. (c) Gibbs free energy profile of the HER on various models.

rapid electron transfer channels and a synergistic coupling effect on the electron distribution, which will be very beneficial for the improvement in HER performance. Generally, the Gibbs free energy (ΔG_{H*}) of hydrogen adsorbed on the catalyst surface is usually used to evaluate HER catalyst activity [53]. A superior candidate catalyst for HER should have ΔG_{H*} close to 0 to maintain a balance between the transfer of H$^+$ and removal of H* [54]. As summarized in Fig. 5c, the free energies of H* adsorption on the CoSe$_2$ alloy, pure NG, and CoSe$_2$ @NG model are 0.581, − 2.624, and − 0.349 eV, respectively. CoSe$_2$ @NG model exhibited the smallest $|\Delta G_{H*}|$ value, indicating it has the most suitable H* adsorption and desorption steps, resulting in high HER activity, matching well with the experimental results.

3.4. Hydrophilic and aerophobicity characterization

The wettability and surface hydrophilicity of the electrode are one of the key factors that influence the catalytic activity of electrocatalysts [29]. Here, the contact angles (CAs) measurement was conducted to quantitatively analyze the wettability of these as-prepared samples. Commercial CC shows unsatisfactory hydrophilicity, the water-drops can stay on the surface and hardly penetrate into the interior (Fig. S16a). The measured CAs are 130°, as well proves the bad wettability of commercial CC. For CC/CS-As and CC/NG-HCS@NGM-As samples, when the water dropped onto the surface, water drops diffuse instantaneously (only tens or hundreds of milliseconds) and pump into the electrode by a strong capillary force, indicating the remarkable electrolyte wettability (Fig. S16b and c). The improvement of hydrophilicity from less wettable commercial CC to superhydrophilic CC/CS-As and CC/NG-HCS@NGM-As indicates that coupling rugged morphology electroactive material with inert CC substrate can remold unique surface characteristic of the integrated electrode and ensure

accessibility of the active sites to electrolytes. Furthermore, The CC/NG-HCS@NGM-As shows a shorter infiltration time and its electrolytes affinity and mass transfer ability surpasses that of the CC/CS-As, which may benefit from the nanopores in graphene nanomesh and the surface hydrophilic groups of N-doped graphene.

During the HER process, if the generated hydrogen bubbles cannot be quickly removed, they will adhere or aggregate on the electrocatalyst surface, seriously reducing the contact area between active sites and reactants [39]. Generally, in the gas evolution reaction, the bubble release can be accelerated by increasing the bubble contact angle and reducing the size of the bubble during separation [29]. Therefore, constructing unique "superaerophobic" characteristics may effectively achieve these goals. The surface aerophobicity of electrocatalysts is generally evaluated by the receding contact angle measurement. The smaller the receding contact angle, the easier the gas bubble detached from the catalytic surface. Fig. S16d shows the receding contact angle of those samples. Compared with the angles of commercial CC was 120°, the CC/CS-As exhibit improved value of 9.2°, and the CC/NG-HCS@NGM-As show the minimum angles of only 6.2°. Furthermore, the adhesion behavior of gas bubbles was studied (Fig. S16e), representing that air bubbles can also be quickly and easily released from the surface of CC/NG-HCS@NGM-As in a short time of 230 ms. These results indicate that the 3D GM-As structure provides superaerophobic surface that enables rapid gas release, resulting in enhanced electrocatalytic activity. To further investigate the ability of these catalysts to re-expose active sites to the electrolyte, we recorded the digital photography to count the size distributions of the releasing hydrogen bubble on different samples. Clearly, the diameters of the released bubbles from bare CC (Fig. S16f), CC/CS-As (Fig. S16g), and CC/NG-HCS@NGM-As (Fig. S16h) electrodes can be expressed as ~86% are larger than 100 μm and some are larger than 400 μm, ~74% are in

the range of 100–200 μm, and all are smaller than 200 μm and ~62% are in the range of 50–100 μm, respectively. The bubble releasing manner of CC/NG-HCS@NGM-As ensures the fast and constant re-exposure of catalytic sites to the surrounding electrolyte. As illustrated in Fig. S16i, based on the solid-liquid-gas interface theory [20], the hierarchical structure with microscopic/nanoscopic roughness in CC/NG-HCS@NGM-As electrode not only generates strong capillary force to pump electrolyte, but also reduces the contact sites to expedite gas bubble detaching, thereby accelerating the hydrogen evolution reaction kinetics.

3.5. Finite element simulation and analysis

The rapid mass transfer of catalysts plays a vital role in activity enhancement, which is closely related to their mircomorphology [55]. Previous studies proved that self-supporting nanosheet arrays architectures have more efficient mass transfer abilities than powder/bulk morphology [56]. As the basic constituent unit of the 3D GM arrays, graphene nanomeshes with a high-density of in plane nanopores on their conjugated skeletons. Such pores provide abundant channels for species propagation along Z-axis. Therefore, we speculate that the mass transfer efficiency of the integrated electrodes will be further enhanced by the in-plane nanopores. To verify this conjecture, we used the finite element analysis (FEA) method to explore the influence of in-plane pores on the ion flux distribution at the nanometer scale. FEA is an effective method to solve some engineering problems in the fields of traditional material transport and electrochemical reactions [57]. Abstracting from the morphology size and pore size distribution results by SEM, TEM, and BET characterization of the CC/NG-HCS@NGM-As sample, the model of 3D GM-As based on the geometries with a height, length, width and pore diameter of 6 μm, 1 μm, 1 μm, and 50/100 nm respectively were constructed. The bare nanosheet arrays without pores was used as the control (Fig. 6a). The reaction pathway of HER in alkaline medium is

$2 H_2O + 2e^- \rightarrow H_2 + 2OH^-$. The electrode surface reaction process is based on the Butler-Volmer equation, and the OH^- flux in the electrolyte at steady state is calculated by coupling the electrochemical current distribution and the mass transfer process. The simulated fluxes of OH^- shows the local diffusion of reactants per second associated with the consumption rate. Fig. 6b displays the cross-sectional distribution of OH^- flux in three models. In the nanosheet array (without pore) model, due to the surrounding sealing features of the nanosheets, the OH^- flux presents an uneven distribution, leading to the inability to fully utilize the large-spaced underlying sites. For both the nanomesh array models with pore diameter of 50 nm and 100 nm, the overall OH^- flux is dramatically increased, allowing the sites at the bottom to be efficiently utilized. Especially at the upper region of the arrays, the nanomesh array model represents higher OH^- flux. This reason is that when the in-plane pores appear, OH^- ions have more channels to pass directly improving the flux. Fig. 6c digitizes the changes in OH^- fluxes to facilitate visual comparison. At any location within the array's interior space, the numerical value of the nanomesh array model is significantly larger than that of the nanosheet array model. Collectively, the above results prove that the introduction of in-plane pores can greatly improve the OH^- flux, promoting the transport of substances. In addition, we also investigated the surface OH^- ion concentration distribution of the three models (Fig. S17). Since the introduction of in-plane nanopores neither changes the entire geometry of these models nor brings structures such as tips with local electric field enhancement effects [58], the surface OH^- concentration distributions of the three models are basically the same, without obvious aggregation.

According to the above investigation, the CC/NG-HCS@NGM-As electrode exhibited excellent HER activity, which can be explained by the integrative merits of several aspects as follows (Fig. S18): (1) The strong interfacial interaction between NG and $CoSe_2$ can accelerate the charge-transfer/penetration dynamics, as well as weaken H* adsorption. (2) The NG layers coated on the outer surface of hollow
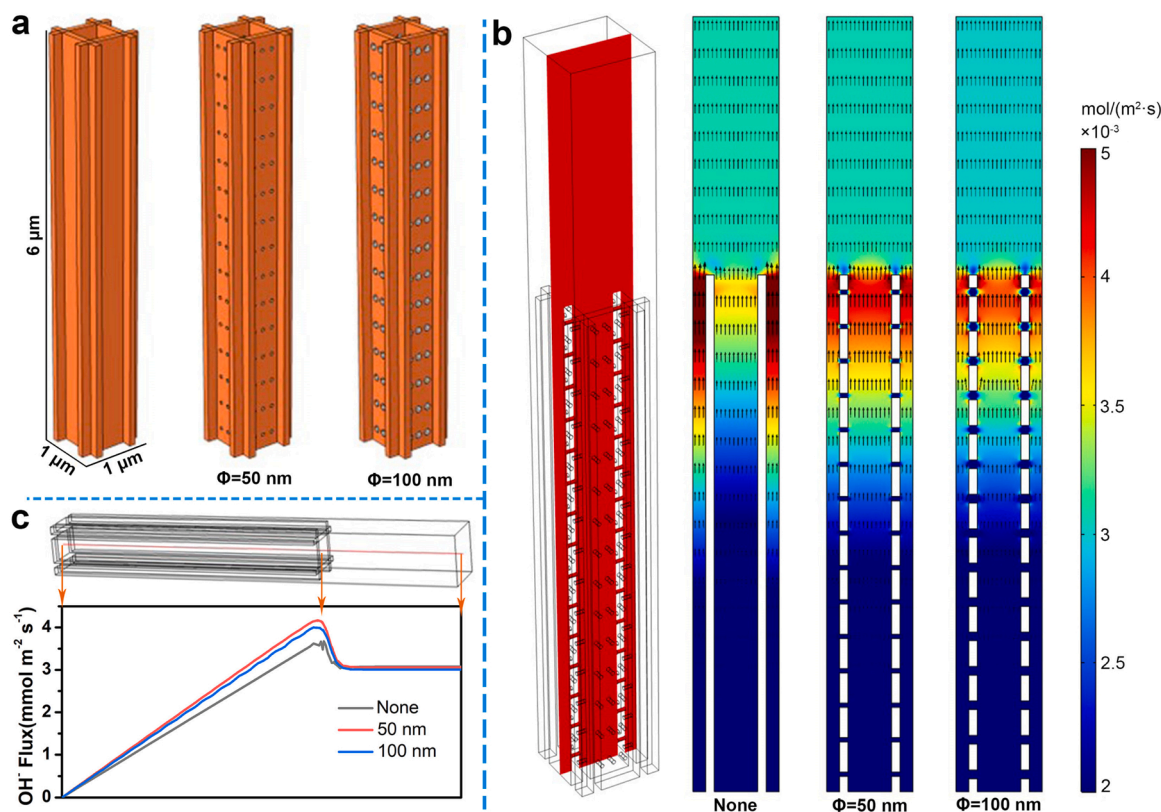

Fig. 6. (a) Three geometric models, including nanosheet arrays, nanomesh arrays with pore diameter of 50 nm and 100 nm. (b) The corresponding flux profile of OH^- for the HER on three models obtained with finite element simulations. (c) Specific numerical curves of OH^- fluxes for different models.

CoSe$_2$ microspheres act as "confined space," which can effectively prevent CoSe$_2$ active components from pulverization and/or loss under harsh media during the long term practical usage. (3) The uniform NGM arrays on CC provide a perpetual and robust conductive platform; the highly conductive NG matrix shell ensures that electrons can transfer through the NGM-As to the active CoSe$_2$ nanoparticles, resulting in fast electron transport through the entire electrode. (4) The 3D vertically oriented N-doped graphene nanomesh arrays structure not only maximizes the electrode/electrolyte contact and exposes more catalytic active sites, but also improves ion diffusion by shortening the pathways. (5) Such a self-supporting integrated electrode does not require additional binders and conductive additives. The robust contact between NG-HCS@NGM-As and the CC substrate augments the electrochemical activity and stability. Thus, it is demonstrated that integrated fabrication and multi-component synergistic cooperation are effective means to obtain high-performance HER electrodes.

4. Conclusion

To summarize, we meticulously designed a facile strategy to synthesize N-doped graphene confined hollow CoSe$_2$ nanoparticles @N-doped vertically oriented graphene nanomesh arrays grown on carbon cloth (CC/NG-HCS@NGM-As). The obtained CC/NG-HCS@NGM-As was employed as an efficient electrocatalyst for HER with superior activity, such as a low overpotential of 133 mV at current density of 10 mA cm^{-2}, a small Tafel slope of 80.5 mV dec^{-1}, and a high TOF value of 0.15 s^{-1}. Such excellent catalytic performance can be attributed to the integrated construction and synergistic cooperation of the nanostructural design and electronic structure modulation. DFT calculation reveals that the electron redistribution at the engineered CoSe$_2$ @NG confined interfaces optimizes the adsorption energy of H* for HER process. Also, the surface properties measurement and finite element analysis verify the 3D graphene nanomesh arrays facilitate OH$^-$ and gas transport and active sites exposure. Undoubtedly, this study provides a promising route to design and manufacture electrocatalysts for water splitting.

CRediT authorship contribution statement

Kai Chi, Zhu Wu: Contributed equally to this work. **Kai Chi**: Methodology, Investigation, Data curation, Conceptualization, Formal analysis, Validation, Writing – original draft. **Zhu Wu**: Conceptualization, Visualization, Investigation, Formal analysis, Writing – original draft. **Xin Tian**: Software. **Zhuoping Wang**: Formal analysis. **Fei Xiao**: Data curation, Visualization. **Junwu Xiao**: Formal analysis, Supervision. **Shuai Wang**: Writing – review & editing, Funding acquisition, Supervision, Project administration.

Declaration of Competing Interest

The authors declare that they have no known competing financial interests or personal relationships that could have appeared to influence the work reported in this paper.

Data availability

Data will be made available on request.

Acknowledgments

Appendix A. Supporting information

Supplementary data associated with this article can be found in the online version at doi:10.1016/j.apcatb.2022.122256.

References

[1] J. Zhu, L. Hu, P. Zhao, L.Y. Suk Lee, K.-Y. Wong, Recent advances in electrocatalytic hydrogen evolution using nanoparticles, Chem. Rev. 120 (2020) 851–918, https://doi.org/10.1021/acs.chemrev.9b00248.

[2] M.F. Lagadec, A. Grimaud, Water electrolysers with closed and open electrochemical systems, Nat. Mater. 19 (2020) 1140–1150, https://doi.org/10.1038/s41563-020-0788-3.

[3] Y. Wu, W. Wei, R. Yu, L. Xia, X. Hong, J. Zhu, J. Li, L. Lv, W. Chen, Y. Zhao, L. Zhou, L. Mai, Anchoring sub-nanometer Pt clusters on crumpled paper-like MXene enables high hydrogen evolution mass activity, Adv. Funct. Mater. 32 (2022), 2110910, https://doi.org/10.1002/adfm.202110910.

[4] Z. Wei, B. Li, C. Xia, Y. Cui, J. He, J.-B. Xia, J. Li, Various structures of 2D transition-metal dichalcogenides and their applications, Small Methods 2 (2018), 1800094, https://doi.org/10.1002/smtd.201800094.

[5] X. Xia, L. Wang, N. Sui, V.L. Colvinc, W.W. Yu, Recent progress in transition metal selenide electrocatalysts for water splitting, Nanoscale 12 (2020) 12249–12262, https://doi.org/10.1039/D0NR02939D.

[6] Y. Sun, K. Xu, Z. Wei, H. Li, T. Zhang, X. Li, W. Cai, J. Ma, H.J. Fan, Y. Li, Strong electronic interaction in dual-cation-incorporated NiSe$_2$ nanosheets with lattice distortion for highly efficient overall water splitting, Adv. Mater. 30 (2018), 1802121, https://doi.org/10.1002/adma.201802121.

[7] Y. Yin, Y. Zhang, T. Gao, T. Yao, X. Zhang, J. Han, X. Wang, Z. Zhang, P. Xu, P. Zhang, X. Cao, B. Song, S. Jin, Synergistic phase and disorder engineering in 1T-MoSe$_2$ nanosheets for enhanced hydrogen-evolution reaction, Adv. Mater. 29 (2017), 1700311, https://doi.org/10.1002/adma.201700311.

[8] B. Wang, Z. Wang, X. Wang, B. Zheng, W. Zhang, Y. Chen, Scalable synthesis of porous hollow CoSe$_2$–MoSe$_2$/carbon microspheres for highly efficient hydrogen evolution reaction in acidic and alkaline media, J. Mater. Chem. A 6 (2018) 12701–12707, https://doi.org/10.1039/C8TA03523G.

[9] X. Wang, B. Zheng, B. Yu, B. Wang, W. Hou, W. Zhang, Y. Chen, In situ synthesis of hierarchical MoSe$_2$–CoSe$_2$ nanotubes as an efficient electrocatalyst for the hydrogen evolution reaction in both acidic and alkaline media, J. Mater. Chem. A 6 (2018) 7842–7850, https://doi.org/10.1039/C8TA01552J.

[10] X. Wang, B. Zheng, B. Wang, H. Wang, B. Sun, J. He, W. Zhang, Y. Chen, Hierarchical MoSe$_2$-CoSe$_2$ nanotubes anchored on graphene nanosheets: A highly efficient and stable electrocatalyst for hydrogen evolution in alkaline medium, Electrochim. Acta 299 (2019) 197–205, https://doi.org/10.1016/j.electacta.2018.12.101.

[11] X. Wang, J. He, B. Yu, B. Sun, D. Yang, X. Zhang, Q. Zhang, W. Zhang, L. Gu, Y. Chen, CoSe$_2$ nanoparticles embedded MOF-derived Co-N-C nanoflake arrays as efficient and stable electrocatalyst for hydrogen evolution reaction, Appl. Catal. B: Environ. 258 (2019), 117996, https://doi.org/10.1016/j.apcatb.2019.117996.

[12] W. Zhou, J. Lu, K. Zhou, L. Yang, Y. Ke, Z. Tang, S. Chen, CoSe$_2$ nanoparticles embedded defective carbon nanotubes derived from MOFs as efficient electrocatalyst for hydrogen evolution reaction, Nano Energy 28 (2016) 143–150, https://doi.org/10.1016/j.nanoen.2016.08.040.

[13] H. Yue, B. Yu, F. Qi, J. Zhou, X. Wang, B. Zheng, W. Zhang, Y. Li, Y. Chen, Interwoven CoSe$_2$/CNTs hybrid as a highly efficient and stable electrocatalyst for hydrogen evolution reaction, Electrochim. Acta 253 (2017) 200–207, https://doi.org/10.1016/j.electacta.2017.09.066.

[14] K. Zhou, J. He, X. Wang, J. Lin, Y. Jing, W. Zhang, Y. Chen, Self-assembled CoSe$_2$ nanocrystals embedded into carbon nanowires as highly efficient catalyst for hydrogen evolution reaction, Electrochim. Acta 231 (2017) 626–631, https://doi.org/10.1016/j.electacta.2017.02.089.

[15] T. Kou, S. Wang, Y. Li, Perspective on high-rate alkaline water splitting, ACS Mater. Lett. 3 (2021) 224–234, https://doi.org/10.1021/acsmaterialslett.0c00536.

[16] M. Jin, X. Zhang, S. Niu, Q. Wang, R. Huang, R. Ling, J. Huang, R. Shi, A. Amini, C. Cheng, Strategies for designing high-performance hydrogen evolution reaction electrocatalysts at large current densities above 1000 mA cm^{-2}, ACS Nano 16 (2022) 11577–11597, https://doi.org/10.1021/acsnano.2c02820.

[17] X. Yu, Z.-Y. Yu, X.-L. Zhang, Y.-R. Zheng, Y. Duan, Q. Gao, R. Wu, B. Sun, M.-R. Gao, G. Wang, S.-H. Yu, "Superaerophobic" nickel phosphide nanoarray catalyst for efficient hydrogen evolution at ultrahigh current densities (https://pubs.acs.org/doi/), J. Am. Chem. Soc. 141 (2019) 7537–7543, https://doi.org/10.1021/jacs.9b02527.

[18] L. Zhang, J. Zhang, J. Fang, X.-Y. Wang, L. Yin, W. Zhu, Z. Zhuang, Cr-doped CoP nanorod arrays as high-performance hydrogen evolution reaction catalysts at high current density, Small 17 (2021), 2100832, https://doi.org/10.1002/smll.202100832.

[19] Q. Gao, W. Zhang, Z. Shi, L. Yang, Y. Tang, Structural design and electronic modulation of transition-metal-carbide electrocatalysts toward efficient hydrogen evolution, Adv. Mater. 31 (2019), 1802880, https://doi.org/10.1002/adma.201802880.

[20] Y. Luo, L. Tang, U. Khan, Q. Yu, H.-M. Cheng, X. Zou, B. Liu, Morphology and surface chemistry engineering toward pH-universal catalysts for hydrogen evolution at high current density, Nat. Commun. 10 (2019) 269, https://doi.org/10.1038/s41467-018-07792-9.

[21] H. Sun, Z. Yan, C. Tian, C. Li, X. Feng, R. Huang, Y. Lan, J. Chen, C.-P. L, Z. Zhang, M. Du, Bixbyite-type Ln2O3 as promoters of metallic Ni for alkaline electrocatalytic hydrogen evolution, Nat. Commun. 13 (22) 3857. https://doi.org/10.1038/s41467-022-31561-4.

[22] G. Zhao, K. Rui, S.X. Dou, W. Sun, Heterostructures for electrochemical hydrogen evolution reaction: a review, Adv. Funct. Mater. 28 (2018), 1803291, https://doi.org/10.1002/adfm.201803291.

[23] X. Wang, R.K.M. Raghupathy, C.J. Querebillo, Z. Liao, D. Li, K. Lin, M. Hantusch, Z. Sofer, B. Li, E. Zschech, I.M. Weidinger, T.D. Kühne, H. Mirhosseini, M. Yu, X. Feng, Interfacial covalent bonds regulated electron-deficient 2D black phosphorus for electrocatalytic oxygen reactions, Adv. Mater. 33 (2021), 2008752, https://doi.org/10.1002/adma.202008752.

[24] H. Tabassum, A. Mahmood, B. Zhu, Z. Liang, R. Zhong, S. Guo, R. Zou, Recent advances in confining metal-based nanoparticles into carbon nanotubes for electrochemical energy conversion and storage devices, Energy Environ. Sci. 12 (2019) 2924–2956, https://doi.org/10.1039/C9EE00315K.

[25] L.-P. Yuan, T. Tang, J.-S. Hu, L.-J. Wan, Confinement strategies for precise synthesis of efficient electrocatalysts from the macroscopic to the atomic level, Acc. Mater. Res. 2 (2021) 907–919, https://doi.org/10.1021/accountsmr.1c00135.

[26] J. Deng, P. Ren, D. Deng, X. Bao, Enhanced electron penetration through an ultrathin graphene layer for highly efficient catalysis of the hydrogen evolution reaction, Angew. Chem. Int. Ed. 54 (2015) 2100–2104, https://doi.org/10.1002/anie.201409524.

[27] L. Yu, D. Deng, X. Bao, Chain mail for catalysts, Angew. Chem. Int. Ed. 59 (2020) 15294–15297, https://doi.org/10.1002/anie.202007604.

[28] S. Zhang, W. Wang, F. Hu, Y. Mi1, S. Wang, Y. Liu, X. Ai, J. Fang, H. Li, T. Zhai, 2D CoOOH sheet-encapsulated Ni2P into tubular arrays realizing 1000 mA cm⁻² -level-current-density hydrogen evolution over 100h in neutral water, Nano-Micro Lett. 12 (2020) 140, https://doi.org/10.1007/s40820-020-00476-4.

[29] W. Xu, Z. Lu, X. Sun, L. Jiang, X. Duan, Superwetting electrodes for gas-involving electrocatalysis (https://pubs.acs.org/doi/), Acc. Chem. Res 51 (2018) 1590–1598, https://doi.org/10.1021/acs.accounts.8b00070.

[30] Z. Huang, S. Yuanb, T. Zhang, B. Cai, B. Xu, X. Lu, L. Fan, F. Dai, D. Sun, Selective selenization of mixed-linker Ni-MOFs: NiSe2@NC core-shell nanooctahedrons with tunable interfacial electronic structure for hydrogen evolution reaction, Appl. Catal. B: Environ. 272 (2020), 118976, https://doi.org/10.1016/j.apcatb.2020.118976.

[31] M. Yi, B. Lu, X. Zhang, Y. Tan, Z. Zhu, Z. Pan, J. Zhang, Ionic liquid-assisted synthesis of nickel cobalt phosphide embedded in N, P codoped-carbon with hollow and folded structures for efficient hydrogen evolution reaction and supercapacitor, Appl. Catal. B: Environ. 283 (2021), 119635, https://doi.org/10.1016/j.apcatb.2020.119635.

[32] S. Wan, W. Jin, X. Guo, J. Mao, L. Zheng, J. Zhao, J. Zhang, H. Liu, C. Tang, Self-templating construction of porous CoSe2 nanosheet arrays as efficient bifunctional electrocatalysts for overall water splitting, ACS Sustain. Chem. Eng. 6 (2018) 15374–15382, https://doi.org/10.1021/acssuschemeng.8b03804.

[33] C. Liang, P. Zou, A. Nairan, Y. Zhang, J. Liu, K. Liu, S. Hu, F. Kang, H.J. Fan, C. Yang, Exceptional performance of hierarchical Ni–Fe oxyhydroxide@NiFe alloy nanowire array electrocatalysts for large current density water splitting, Energy Environ. Sci. 13 (2020) 86–95, https://doi.org/10.1039/C9EE02388G.

[34] L. Li, W. Liu, H. Dong, Q. Gui, Z. Hu, Y. Li, J. Liu, Surface and interface engineering of nanoarrays toward advanced electrodes and electrochemical energy storage devices, Adv. Mater. 33 (2021), 2004959, https://doi.org/10.1002/adma.202004959.

[35] J.M. Ibrahim, X. Sun, Recent progress on earth abundant electrocatalysts for hydrogen evolution reaction (HER) in alkaline medium to achieve efficient water splitting –A review, J. Energy Chem. 34 (2019) 111–160, https://doi.org/10.1016/j.jechem.2018.09.016.

[36] Y. Song, J. Cheng, J. Liu, Q. Ye, X. Gao, J. Lu, Y. Cheng, Modulating electronic structure of cobalt phosphide porous nanofiber by ruthenium and nickel dual doping for highly-efficiency overall water splitting at high current density, Appl. Catal. B: Environ. 298 (2021), 120488, https://doi.org/10.1016/j.apcatb.2021.120488.

[37] H. Sun, Z. Yan, F. Liu, W. Xu, F. Cheng, J. Chen, Self-supported transition-metal-based electrocatalysts for hydrogen and oxygen evolution, Adv. Mater. 32 (2020), 1806326, https://doi.org/10.1002/adma.201806326.

[38] X. Shan, J. Liu, H. Mu, Y. Xiao, B. Mei, W. Liu, G. Lin, Z. Jiang, L. Wen, L. Jiang, An engineered superhydrophilic/superaerophobic electrocatalyst composed of the supported CoMoSₓ chalcogel for overall water splitting, Angew. Chem. Int. Ed. 59 (2020) 1659–1665, https://doi.org/10.1002/anie.201911617.

[39] Y. Luo, Z. Zhang, F. Yang, J. Li, Z. Liu, W. Ren, S. Zhang, B. Liu, Stabilized hydroxide-mediated nickel-based electrocatalysts for high-current-density hydrogen evolution in alkaline media, Energy Environ. Sci. 14 (2021) 4610–4619, https://doi.org/10.1039/D1EE01487K.

[40] Z. Bo, S. Mao, Z.J. Han, K. Cen, J. Chen, K. (K.) Ostrikov, Emerging energy and environmental applications of vertically-oriented graphenes, Chem. Soc. Rev. 44 (2015) 2108–2121, https://doi.org/10.1039/C4CS00352G.

[41] Z. Zhang, C.-S. Lee, W. Zhang, Vertically aligned graphene nanosheet arrays: synthesis, properties and applications in electrochemical energy conversion and storage, Adv. Energy Mater. 7 (2017), 1700678, https://doi.org/10.1002/aenm.201700678.

[42] K. Chi, Z. Chen, F. Xiao, W. Guo, W. Xi, J. Liu, H. Yan, Z. Zhang, J. Xiao, J. Liu, J. Luo, S. Wang, K.P. Loh, Maximizing the utility of single atom electrocatalysts on a 3D graphene nanomesh, J. Mater. Chem. A 7 (2019) 15575–15579, https://doi.org/10.1039/C9TA00942F.

[43] J. Zhu, W. Tu, H. Pan, H. Zhang, B. Liu, Y. Cheng, Z. Deng, H. Zhang, Self-templating synthesis of hollow Co3O4 nanoparticles embedded in N,S-dual-doped reduced graphene oxide for lithium ion batteries, ACS Nano 14 (2020) 5780–5787, https://doi.org/10.1021/acsnano.0c00712.

[44] J. Tian, J. Li, Y. Zhang, X.-Y. Yu, Z. Hong, Carbon-coated CoSe2 nanoparticles confined in N-doped carbon microboxes with enhanced sodium storage properties, J. Mater. Chem. A 7 (2019), 21404, https://doi.org/10.1039/C9TA06273D.

[45] Y. Tang, Z. Zhao, X. Hao, Y. Wang, Y. Liu, Y. Hou, Q. Yang, X. Wang, J. Qiu, Engineering hollow polyhedrons structured from carbon-coated CoSe2 nanospheres bridged by CNTs with boosted sodium storage performance, J. Mater. Chem. A 5 (2017) 13591–13600, https://doi.org/10.1039/C7TA02665J.

[46] M.S. Jo, J.S. Lee, S.Y. Jeong, J.K. Kim, Y.C. Kang, S.M. Jeong, J.S. Cho, Golden bristlegrass-like hierarchical graphene nanofibers entangled with N-doped CNTs containing CoSe2 nanocrystals at each node as anodes for high-rate sodium-ion batteries, Small 16 (2020), 2003391, https://doi.org/10.1002/smll.202003391.

[47] S.H. Yang, S.-K. Park, Y.C. Kang, Mesoporous CoSe2 nanoclusters threaded with nitrogen-doped carbon nanotubes for high-performance sodium-ion battery anodes, Chem. Eng. J. 370 (2019) 1008–1018, https://doi.org/10.1016/j.cej.2019.03.263.

[48] B. Li, Y. Liu, X. Jin, S. Jiao, G. Wang, B. Peng, S. Zeng, L. Shi, J. Li, G. Zhang, Designed formation of hybrid nanobox composed of carbon sheathed CoSe2 anchored on nitrogen-doped carbon skeleton as ultrastable anode for sodium-ion batteries, Small 15 (2019), 1902881, https://doi.org/10.1002/smll.201902881.

[49] E. Xu, P. Li, J. Quan, H. Zhu, L. Wang, Y. Chang, Z. Sun, L. Chen, D. Yu, Y. Jiang, Dimensional gradient structure of CoSe2@CNTs–MXene anode assisted by ether for high-capacity, stable sodium storage, Nano-Micro Lett. 13 (2021) 40, https://doi.org/10.1007/s40820-020-00562-7.

[50] S.H. Yang, S.-K. Park, Y.C. Kang, MOF-derived CoSe2@N-doped carbon matrix confined in hollow mesoporous carbon nanospheres as high-performance anodes for potassium-ion batteries, Nano-Micro Lett. 13 (2021) 9, https://doi.org/10.1007/s40820-020-00539-6.

[51] Z. Hou, C. Shu, R. Zheng, C. Liu, Z. Ran, T. Yang, P. Hei, Q. Zhang, J. Long, Anionic vacancy-dependent activity of the CoSe2 with a tunable interfacial electronic structure on the N-doped carbon cloth for advanced Li–O2 batteries, J. Mater. Chem. A 8 (2020) 16636–16648, https://doi.org/10.1039/D0TA05117A.

[52] B. Li, B. Xi, Z. Feng, Y. Lin, J. Liu, J. Feng, Y. Qian, S. Xiong, Hierarchical porous nanosheets constructed by graphene-coated, interconnected TiO2 nanoparticles for ultrafast sodium storage, Adv. Mater. 30 (2018), 1705788, https://doi.org/10.1002/adma.201705788.

[53] Z. Huang, B. Xu, Z. Li, J. Ren, H. Mei, Z. Liu, D. Xie, H. Zhang, F. Dai, R. Wang, D. Sun, Accurately regulating the electronic structure of NixSey@NC core–shell nanohybrids through controllable selenization of a Ni-MOF for pH-universal hydrogen evolution reaction, Small 16 (2020), 2004231, https://doi.org/10.1002/smll.202004231.

[54] Y. Liu, G. Yu, G.-D. Li, Y. Sun, T. Asefa, W. Chen, X. Zou, Coupling Mo2C with nitrogen-rich nanocarbon leads to efficient hydrogen-evolution electrocatalytic sites, Angew. Chem. Int. Ed. 54 (2015) 10752–10757, https://doi.org/10.1002/anie.201504376.

[55] J. Wang, N. Zang, C. Xuan, B. Jia, W. Jin, T. Ma, Self-supporting electrodes for gas-involved key energy reactions, Adv. Funct. Mater. 31 (2021), 2104620, https://doi.org/10.1002/adfm.202104620.

[56] H. Yang, M. Driess, P.W. Menezes, Self-supported electrocatalysts for practical water electrolysis, Adv. Energy Mater. 11 (2021), 2102074, https://doi.org/10.1002/aenm.202102074.

[57] P. Li, Z. Jin, Z. Fang, G. Yu, A surface-strained and geometry-tailored nanoreactor that promotes ammonia electrosynthesis, Angew. Chem. Int. Ed. 59 (2020) 22610–22616, https://doi.org/10.1002/anie.202011596.

[58] P. Liu, B. Chen, C. Liang, W. Yao, Y. Cui, S. Hu, P. Zou, H. Zhang, H.J. Fan, C. Yang, Tip-enhanced electric field: a new mechanism promoting mass transfer in oxygen evolution reactions, Adv. Mater. 33 (2021), 2007377, https://doi.org/10.1002/adma.202007377.